Journal of Power Sources 624 (2024) 235537

Contents lists available at ScienceDirect

Journal of Power Sources

journal homepage: www.elsevier.com/locate/jpowsour

High protonic resistance of hydrocarbon-based cathodes in PEM fuel cells under low humidity conditions: Origin, implication, and mitigation

Hannes Liepold [a,b], Ashley Bird [c], Philipp A. Heizmann [a], Hassan Fadlullah [d], Hien Nguyen [d], Carolin Klose [a], Steven Holdcroft [e], Ahmet Kusoglu [c], Severin Vierrath [a,b], Andreas Münchinger [a,d,*]

[a] Electrochemical Energy Systems, Department of Microsystems Engineering (IMTEK), University of Freiburg, Georges-Koehler-Allee 103, 79110, Freiburg, Germany
[b] Freiburg Materials Research Center (FMF), University of Freiburg, Stefan-Meier-Straße 21, 79104, Freiburg, Germany
[c] Energy Conversion Group, Energy Technologies Area, Lawrence Berkeley National Laboratory, Berkeley, CA, 94720, USA
[d] Hahn-Schickard, Georges-Koehler-Allee 103, 79110, Freiburg, Germany
[e] Department of Chemistry, Simon Fraser University, Burnaby, BC, V5A 1S6, Canada

HIGHLIGHTS

- First thin film (22 nm) measurements on sulfonated phenylated polyphenylenes.
- Evidence on HC ionomer distribution in the CL: Tortuosity, possible pore intrusion.
- Barely any catalyst contribution near the GDL to ORR due to protonic resistance.
- Thin CLs as remediation: 40 % increase in current density at 0.75 V and 50 % RH.

GRAPHICAL ABSTRACT

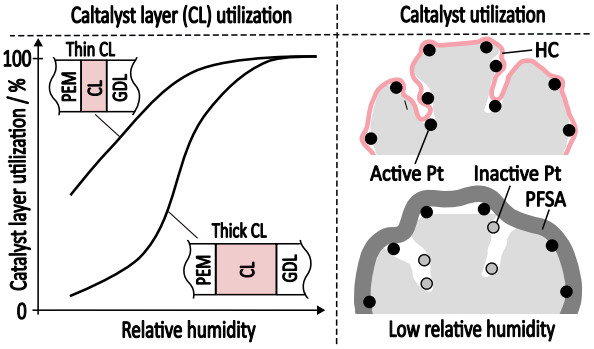

ABSTRACT

Hydrocarbon-based electrodes for proton-exchange membrane fuel cells face challenges in closing the performance gap with electrodes based on perfluorosulfonic acid ionomers, particularly under low humidity conditions. Alongside increased oxygen transport resistance and higher kinetic-induced overpotentials, the protonic resistance of these fluorine-free electrodes is the primary hurdle to improved performance. This study systematically investigates the origin and impact of the cathode protonic resistance on fuel cell performance, utilizing sulfonated phenylated polyphenylenes as hydrocarbon ionomers. Electrochemical characterization at low relative humidity (≤50 %) reveal a high protonic resistance arising from both lower conductivity of the hydrocarbon thin film compared to the bulk membrane and increased cathode tortuosity at a gas transport-optimized ionomer to carbon (I/C) ratio of 0.2. The poor protonic resistance at low relative humidities leads to a non-homogeneous current distribution across the thickness of the cathode electrode, resulting in lower catalyst utilization. To address this issue, reducing the thickness of

* Corresponding author. Electrochemical Energy Systems, IMTEK Department of Microsystems Engineering, University of Freiburg, Georges-Koehler-Allee 103, 79110, Freiburg, Germany.
E-mail address: andreas.muenchinger@imtek.uni-freiburg.de (A. Münchinger).

https://doi.org/10.1016/j.jpowsour.2024.235537
Received 5 August 2024; Received in revised form 15 September 2024; Accepted 25 September 2024
Available online 30 September 2024

the cathode CL while maintaining a constant Pt loading (i.e., increasing the Pt on carbon ratio) significantly reduces protonic resistance. This improvement compensates for the kinetic disadvantages of highly loaded carbon particles and results in a considerable performance increase by 40 % at 0.75 V under low relative humidities.

1. Introduction

State-of-the-art commercially available polymer electrolyte membrane (PEM) fuel cells utilize proton-conductive perfluorosulfonic acid (PFSA) materials, serving as a membrane and a binder in the catalyst layer (CL) [1,2]. However, despite their demonstrated functionality and stability in fuel cells [1], their fluorine-dependent chemistry results in high material cost due to complex synthesis procedures and raises ongoing concerns regarding their environmental impact [3–7]. Hydrocarbon- (HC-) based alternatives offer a promising fluorine-free solution to mitigate these drawbacks. Numerous studies have demonstrated the feasibility of ionomers derived from hydrocarbons when utilized as cation-exchange materials in fully HC-based fuel cells [8–11]. In particular, the class of sulfonated phenylated polyphenylene ionomers was reported to achieve peak performances comparable to long- and short-side-chain PFSA references under H_2/O_2 operation and fully humidified conditions, when employed as unreinforced membrane and proton-conductive binder in the CL [12–14].

Despite the current achievements of the HC research community, the application of the ionomer is hindered by reduced fuel cell performance under targeted automotive conditions (H_2/Air, T > 90 °C), with relative humidity (RH) lower than 50 % [14,15]. This performance limitation can be attributed to two main factors: i) low oxygen reduction reaction (ORR) kinetics and ii) a significant trade-off between high protonic conductivity and low gas transport resistance within the CL. Concerning kinetics, observations reveal reduced mass activities and higher Tafel slopes compared to PFSAs, even after applying optimized HC conditioning processes [16]. This discrepancy may stem from various factors, such as a low electrochemically active surface area (ECSA) [12,17], an increased interaction between Platinum (Pt) and sulfonic acid groups due to high ion exchange capacities (IEC) [18], and potential phenyl poisoning [16]. Being widely known for their low gas permeability [19–21], at low RH, HC-based CLs face the additional challenge of balancing gas transport resistance and ionic resistance. For high surface area carbons, a dry ionomer-to-carbon (I/C) ratio of around 0.2 was found as optimum trade-off, achieving sufficient performance across all current density regions at a high level of humidification (RH ≥ 80 %) [14]. However, under drier conditions, the low I/C ratio leads to a high protonic resistivity of the cathode (e.g., 6.8 kΩ cm at 50 % RH and I/C = 0.2) [15]. The increase in dry ionomer content (i.e., I/C ratio >0.2) reduces the protonic resistance and is speculated to promote a more uniform current distribution within the CL [22]. Nevertheless, at these increased I/C ratios, the in-situ total mass transport resistance in the cathode CL leads to poor performance at high current densities [23]. Nguyen et al. [15] addressed this issue by successfully employing the approach of a gradient ionomer content within the cathode CL. A 30 % reduction in the cathode's protonic resistance was achieved, accompanied by a 35 % increase in current density at 0.7 V.

Given the limitations of the gradient CL approach and the ongoing need for performance enhancements at low RHs, further investigation into the profound impact of protonic conductivity within hydrocarbon CLs is imperative. Previous results suggest a highly non-homogeneous current distribution in the cathode CL, which potentially leads to a reduced Pt utilization at low RHs. This might be attributed to a low protonic conductivity of the binding ionomer thin film and/or its high tortuosity [22,24]. For PFSA-based electrodes, such thin ionomer films cover primary agglomerates within the CL system [25], exhibiting thicknesses between 3 nm and 20 nm [26–28]. Compared to the bulk material, the thin film protonic conductivity was found to be lower [29–31], a discrepancy that is especially pronounced at reduced temperatures (25 °C–30 °C), low relative humidities (<40 %), and thin film thicknesses lower than 55 nm [29–31]. So far, such investigations remain unelucidated for HC materials. Therefore, this study addresses the uncertainties regarding electrode protonic conductivity within fully HC-based fuel cells. The first section involves thin film conductivity measurements, followed by calculating the cathode tortuosity and determining the Pt utilization. The second part of this work proposes and experimentally verifies a remedy to reduce protonic resistance in the cathode CL without increasing mass transport resistance while maintaining the same ionomer content.

2. Experimental

Membrane electrode assembly (MEA) preparation. — Two sulfonated phenylated polyphenylene ionomers were used as protonic conductive materials in the electrodes. A biphenyl-linked sulfonated phenylated polyphenylene (sPPB), supplied by the Holdcroft group (Simon Fraser University, Burnaby, Canada), was utilized in both the anode and cathode to study the effects of protonic conductivity on a fundamental basis. The material was initially reported by Skalski et al. [32] and Adamski et al. [19] with a titrated IEC of 3.19, while it was titrated in this work as 3.3 ± 0.1 meq g^{-1}. For subsequent performance analysis, the commercially available Pemion® PP1-HNN8-00-X (referred to as HNN8) with a titrated IEC in the range of 3.1 ± 0.1 meq g^{-1} was utilized in the anode as well as the cathode. The ionomer was supplied by Ionomr Innovations Inc.

HC catalyst inks were prepared by mixing electrocatalyst, purified water, isopropanol (IPA) and HC ionomer solution (5 wt% ionomer in a 1:1 wt% IPA:H_2O ratio, stirred for 24 h at 40 °C and 260 rpm). The standard Pt on carbon (Pt/C) ratio used for this study was 46.6 wt% (TEC10E50E, Tanaka Kikinzoku Kogyo). For the performance analysis, additional electrocatalysts with Pt/C ratios of 28.3 wt% (TEC10E30E, Tanaka Kikinzoku Kogyo) and 70 wt% (TEC10E70TPM, Tanaka Kikinzoku Kogyo) were employed. Regardless of the electrocatalyst used, the anode's dry ionomer content was maintained at 9 wt%, corresponding to an I/C ratio of 0.2. The cathode's I/C ratio was varied from 0.1 to 0.5 to investigate the effect of effective cathode tortuosity. Regarding the PFSA reference, Nafion (D2020, DuPont) was mixed with 46.6 wt% Pt/C electrocatalyst (TEC10E50E, Tanaka Kikinzoku Kogyo). Based on typical literature values [12,33], the dry ionomer content on both the anode and cathode was maintained at 30 wt%, corresponding to an I/C ratio of 0.8.

An ultrasonic spray system (Sono-Cell®, Sonaer Inc.) was employed to deposit HC inks onto a mechanically-reinforced HC-based Pemion® membrane (PF1-HLF8-15-X, Ionomr Innovations Inc.; 15 μm membrane thickness). For the PFSA reference, a short side-chain Fumapem FS-715-RFS membrane (Fumatech GmbH; 15 μm membrane thickness) was used. All catalyst coated membranes (CCMs) featured a fixed Pt loading on both the anode (0.1 mg_{Pt} cm^{-2}) and cathode (0.4 mg_{Pt} cm^{-2}), determined by micro X-ray fluorescence spectroscopy measurements (μXRF, M4 Tornado, Bruker Corporation). To reduce mechanical failure, the CCMs (4 cm^2 geometric area) were laminated between two polyethylene naphthalate foils (thickness of one foil: 40 μm). Freudenberg H14Cx653 diffusion media and a 5 cm^2 single serpentine flow field (Scribner Associates Inc.) facilitated gas transport to and from the CCMs. A compression ratio of 20 % was achieved by PTFE-coated fiberglass gaskets (thickness of one gasket: 110 μm) and an assembling torque of 10 Nm.

In-situ characterization. — All MEAs were tested on a commercial test stand (850e Fuel Cell Test System, Scribner Associates). All flow

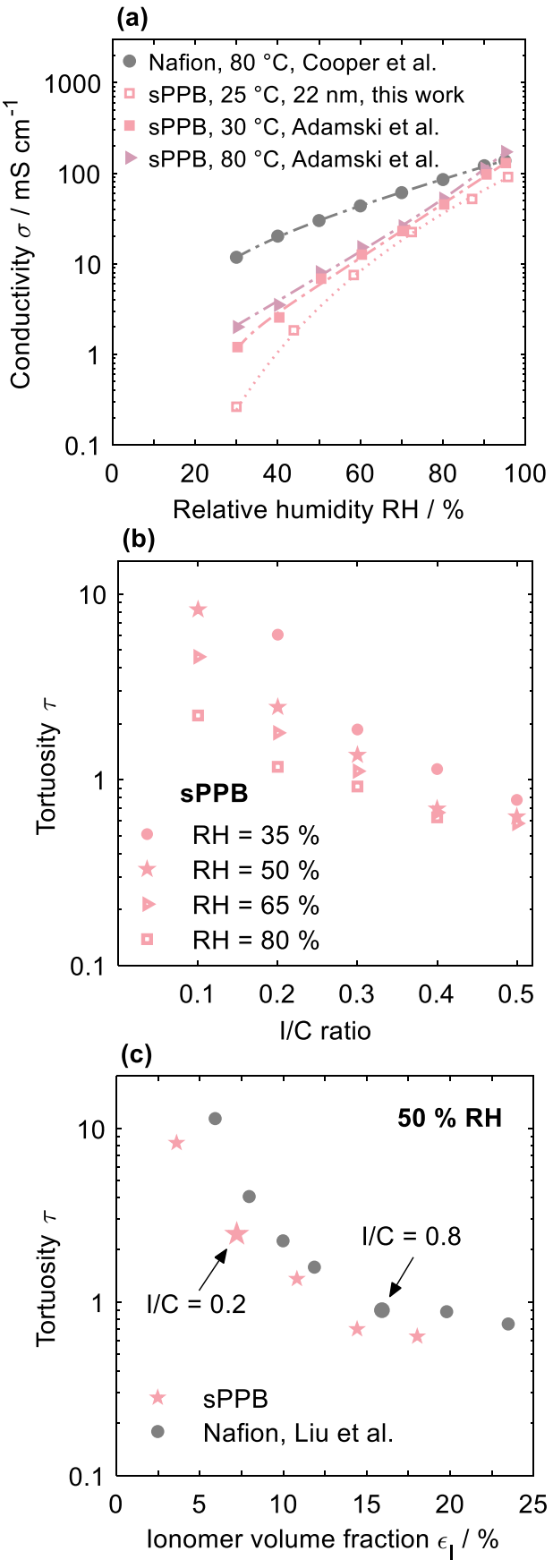

(caption on next column)

Fig. 1. (a) Ex-situ measured in-plane bulk proton conductivities σ (filled data points) for membranes made from sPPB [41] (25 μm, 30 °C and 80 °C) and Nafion NR-212[40] (19 μm, 80 °C). The proton conductivity of the sPPB thin ionomer film (open data points) was measured at room temperature (≈25 °C). The thin film thickness was determined under dry conditions (i.e., 22 nm at 0 % RH). (b) Cathode CL tortuosity τ with respect to the dry sPPB to carbon ratio measured at different RH. τ was calculated from the ex-situ bulk conductivities and in-situ measured protonic impedance resistance (H_2/N_2 measurements) at a fixed temperature of 80 °C. The tortuosity at 35 % RH (I/C = 0.1) and 80 % RH (I/C = 0.5) is not shown, as a data fit with the underlying transmission line model (necessary for evaluating the in-situ conductivity) could not applied within its physically meaningful range. (c) Comparison between this works sPPB-based cathode CL tortuosity and PFSA-based tortuosity [24] with respect to the ionomer volume fraction ϵ_I at 50 % RH. Data points in thick print refer to performance optimized I/C ratios.

rates listed below refer to dry volumetric flows. A voltage-controlled break-in procedure (80 °C, 100 kPa_{abs}, and 96 % RH) was employed, as described in the study by Nguyen et al. [14] No recovery protocol was implemented in this study.

The full characterization starts with determining the ORR kinetics (mass activity and Tafel slope) under H_2/O_2 (0.25 slpm/1.0 slpm) at 80 °C, 96 % RH, and 150 kPa_{abs}. A current-controlled polarization curve was measured from 0 mA cm^{-2} to 95 mA cm^{-2} with a 3-min hold time per point. Data points were collected within two ranges i) 0–30 mA cm^{-2} with steps of 2.5 mA cm^{-2} and ii) 35–95 mA cm^{-2} with steps of 15 mA cm^{-2}. In accordance with the study by Neyerlin et al. [34], the potential was corrected for the high-frequency resistance (HFR) obtained at 3200 Hz. The current was corrected for the hydrogen crossover current and the shorting current of the membrane, both extracted by linear sweep measurements (LSV) with H_2/N_2 (0.20 slpm/0.05 slpm) at 80 °C, 96 % RH, and 150 kPa_{abs}. After applying the corrections, the mass activity equals the Pt loading normalized current density at a potential of 0.9 $V_{HFR\text{-}corrected}$.

The accessible electrochemically surface area (ECSA) was determined via cyclic voltammograms (CVs) by scanning the potential eight times between 0.05 V and 1 V with a scan rate of 50 mV s^{-1}. Beforehand, ten cleaning cycles were applied. Fully humidified (96 % RH) gas flows of H_2/N_2 at 40 °C under ambient pressure were applied, with flow rates of 0.2 slpm for H_2 and 0 slpm for N_2. The ECSA was calculated by normalizing the integrated hydrogen adsorption charge (averaged over the last four cycles) with a specific charge of 210 μC cm^{-2}.

The proton conduction resistance in the cathode was assessed by conducting in-situ AC impedance spectroscopy measurements. 150 kPa_{abs} pressurized flows of H_2/N_2 (0.5 slpm/0.5 slpm) were introduced at five different RHs, starting from 35 % with steps of 15 %. The experiments were conducted using a Gamry Interface 5000E, with an applied voltage of 0.45 V and a frequency range cycled between 0.2 Hz and 100 kHz (20 points per decade). During the investigation phase, the temperature was maintained at 80 °C to facilitate a direct comparison with the ex-situ bulk conductivity reported in literature. Subsequently, the temperature was adjusted to 95 °C to align with the selected operational conditions. The cathodes protonic resistivity was calculated by normalizing the proton conduction resistance with the thickness of the cathode CL, determined by ex-situ cross section measurements (refer to section 'Ex-situ characterization' for more details regarding CL thickness measurements).

H_2/Air (0.25 slpm/1 slpm) polarization curves were measured at 95 °C, 250 kPa_{abs} and RHs of 50 % and 80 %. The current-controlled curves were recorded from low to high current density, with each measurement point held for 3 min (the average of the last 10 s was used).

Ex-situ characterization. — Cross sections of the respective CLs were prepared with a focused ion beam (FIB) scanning electron microscope (FE-SEM, Amber X, Tescan GmbH). Samples were cut in liquid nitrogen and mounted onto standard aluminum SEM stubs (Science Services GmbH) with conductive double-sided adhesive carbon tabs.

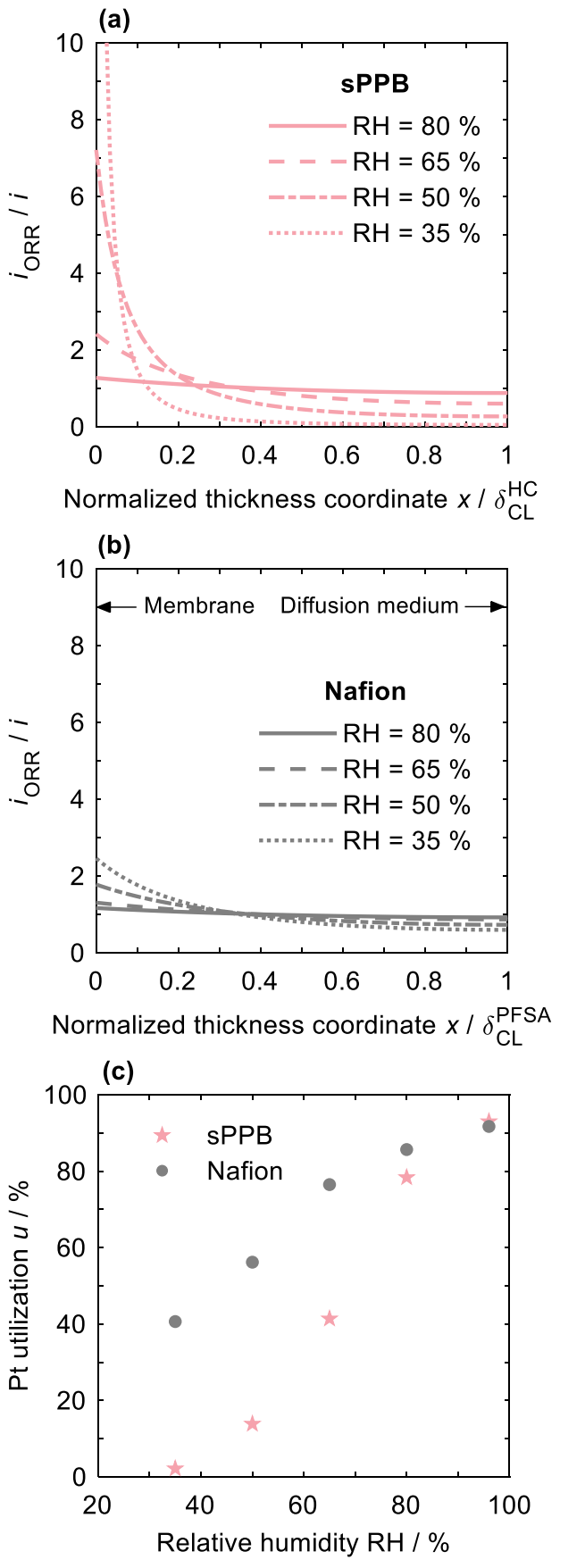

(caption on next column)

Fig. 2. Distribution of i_{ORR} normalized to an average current density $i = 50$ mA cm^{-2} for (a) a fully sPPB-based CCM (I/C = 0.2) or (b) a fully Nafion-based CCM (I/C = 0.8) as a function of the cathode CL thickness coordinate x (i.e., $x = 0$ at the membrane/CL interface and $x = \delta_{Cl}$ at the CL/gas diffusion media interface). For better comparison, x was normalized to the thickness δ_{CL} of the cathode CL. (c) Calculated protonic resistance-induced Pt utilization u over RH for sPPB- and Nafion-based CCMs at 80 °C.

The areas of interest were coated with protective carbon layers using FIB deposition. FIB ablation was then performed by milling over a width of ~100 μm by Xe^+ ions at 20 kV acceleration voltage applying a current of 10 nA, followed by polishing with 100 pA. Micrographs of the catalyst layers were acquired at 2 kV acceleration voltage and a working distance of ~6 mm, with 100 pA current using an Everhart-Thornley (ET) detector. For the quantitative thickness analysis, the micrographs were corrected for the acquisition angle (52°) and segmented using the Trainable Weka Segmentation plugin for ImageJ [35]. After binarizing the micrographs with Weka, the layer thicknesses were determined in steps of 0.05 μm to obtain the presented thickness histograms.

Ionomer thin films were prepared following the procedure explained in Bird et al. [36] Ionomer solutions of 0.5, 1, and 2 wt% sPPB in water and isopropanol (1:1 wt% IPA:H2O ratio) were prepared by stirring at 40 °C for 2–3 h. Custom planar Pt interdigitated electrodes (IDEs) embedded in SiO2 were used as the substrate (see supporting information regarding the procedure on IDE fabrication). Immediately prior to casting, IDEs were rinsed with water, then isopropanol, dried with nitrogen, and plasma-cleaned. sPPB was spun-cast onto the IDE at 3000 rpm for 2 min. Films were then dried at 40 °C for 1 h prior to testing. To measure the film resistance as a function of humidity, the ionomer film was first pre-conditioned by cycling the RH from 0 % to 100 % and back to 0 %. The humidity was then increased from 0 % to 90 % in steps of 15 % and then increased to 100 %. The film was allowed to equilibrate at each RH for 30 min before data collection, with the exception of 100 % RH which equilibrated for 45 min. RH equilibration was performed using a stream of humidified nitrogen. The humidity system (a custom sparging system with two mass flow controllers) and the sample cell holder (allows humidified gas flows) for the custom IDEs were both built in-house. To monitor for leaks, the humidity of the stream was measured downstream of the sample cell using an RH sensor. For electrochemical impedance spectroscopy (EIS) measurements required to extract the film resistance R, two pins in contact with the electrodes were connected to a Biologic potentiostat (VSP-300). The potential oscillation frequency ranged from 0.1 Hz to 1 MHz with an amplitude of 10 mV. Three measurements were collected at each RH, resting 5 min between measurements. Data were collected throughout the experiment, including during RH equilibration at each step. The film was considered equilibrated for IDE measurements when the Nyquist plot exhibited no further changes, indicated by the overlap of at least three consecutive spectra. To extract the film resistance, the spectra were fitted to an appropriate equivalent circuit model that was used in other studies to describe thin films on IDEs [29,36–38]. Based on the film resistance, the thin film proton conductivity σ can be calculated as [36,39]

$$\sigma = \frac{1}{R}\frac{d}{L(N\text{-}1)t} \quad (1)$$

where L denotes the film thickness measured at each humidity using spectroscopic ellipsometry (see supporting information regarding the procedure on thin film thickness measurements). The variables N, d and t refer to the geometry of the IDE (number of teeth, $N = 75$; electrode spacing, $d = 4$ μm; overlapping distance of the electrode teeth, $t = 894$ μm).

3. Results and discussion

HC thin film proton conductivity and cathode tortuosity. —

Table 1
I/C ratio, Pt loading, ECSA and the cathodes CL thickness δ_{CL} for electrodes based on sPPB and Nafion D2020. The protonic resistance $R_{H^+}^{cathode}$ was extracted via H_2/N_2 impedance measurements at 80 °C, 150 kPa_{abs} and 96 % RH. Further electrochemical properties such as mass activity i_m and Tafel slopes (TS) were obtained at 80 °C, 150 kPa_{abs}, 96 % RH under H_2/O_2 configuration. Both electrodes exhibit a Pt/C ratio of 50 wt%.

Ionomer	I/C ratio	i_m (A g_{Pt}^{-1})	TS (mV dec^{-1})	$R_{H^+}^{cathode}$ (m Ω cm^2)	δ_{CL} (μ m)	Pt loading (mg_{Pt} cm^{-2})	ECSA (m^2 g_{Pt}^{-1})
Nafion	0.8	83 ± 5	73 ± 2	81 ± 3	9.7 ± 0.7	0.4 ±0.02	72 ± 2
sPPB	0.2	44 ± 2	76 ± 3	47 ± 2	9.0 ± 0.4	0.4 ±0.01	64 ± 3

Compared to published ex-situ and in-situ measured in- and through-plane data of bulk Nafion [24], [40] sPPB membranes have shown similar in-plane proton conductivities under well-humidified conditions (>90 % RH, 80 °C) [19,41]. However, at application-relevant low RHs, sPPB membranes suffer from a pronounced conductivity drop (Fig. 1a), typical for hydrocarbon membranes [42–44]. In a fully HC-based CCM, this may not only impact the resistance of the bulk membrane but also affect the ionic conductivity of the porous electrode network, where sPPB ionomer is expected to bind the Pt/Carbon agglomerates in the form of a thin film [27]. Due to the absence of extensive 2D transmission electron microscopy studies and ex-situ tomographic measurements, the precise ionomer distribution in thin films, as well as their thickness in HC-based electrodes, remains undetermined and requires further investigation. However, based on local transport resistance measurements [23] and in-situ determined gas crossover of an unreinforced sPPB membrane [19], a possible thin film thickness is calculated to be 2.5 nm (see supporting information for details regarding the calculation). As a spin-cast sPPB film with a thickness of 22 nm (thickness determined under dry conditions, 0 % RH), already shows reduced proton conductivity compared to its bulk membrane (Fig. 1a), thinner films are expected to further continue the trend towards lower conductivity.

At 25 °C, the thin film proton conductivity of a 22 nm sPPB film sharply increases from dry conditions up to 60 % RH, approaching the conductivity of bulk sPPB (measured at 30 °C). In other words, the difference in proton conductivity between the thin ionomer film and bulk material are mainly present at low RHs, with the thin film proton conductivity being two-fold lower at 50 % RH and at 30 % RH even by a factor of 5. The diminished conductivity of such a 22 nm thin film may primarily stem from a reduced water uptake when compared to bulk sPPB (see supporting information, Fig. S1), as well as nanoconfinement effects, influencing various transport parameters (e.g., proton-mobility, dissociated proton concentration, percolation of aqueous ionic domains in nanomorphology, etc.). Similar effects of confinement-driven changes in structure and increase in ion transport resistance have been experimentally found for PFSAs [30,36,45,46].

Irrespective of the precise cause, augmenting the dry ionomer content in the CL of HC fuel cells has been observed to disproportionately decrease protonic CL resistance at low RHs (e.g., RH ≤ 50 %) in comparison to the ionomer volume fraction [15]. It remains unclear whether that decrease originates from "thicker" thin films, which approach bulk properties, or stems from an improved ionomer network, i.e., lower tortuosity. To explore the latter scenario, an analysis of I/C dependent tortuosity τ was conducted, where $\tau = \epsilon_I \sigma_{bulk} \rho_{H^+}$. The cathode tortuosity, representing the complex winding of ion transport pathways [47], was calculated at 80 °C based on the conductivity σ_{bulk} (see Fig. 1) and the in-situ extracted protonic CL resistivity ρ_{H^+} (see supporting information). The ionomer volume fraction ϵ_I includes the water uptake [41] of bulk sPPB at 80 °C. This calculation followed the approach of Neyerlin et al. [34] and Liu et al. [24], considering different I/C ratios and RHs (Fig. 1b). Even at RHs lower than 50 %, the tortuosity remains almost 1 for I/C ratios greater than or equal to 0.4. For lower I/C ratios the tortuosity rises – the drier the conditions, the more pronounced. This increase may be due to disruptions within the ionomer network at low ionomer contents. At desired low RH operation, literature values of Nafion-based cathodes [24] as a function of ionomer volume fraction ϵ_I are slightly higher compared to this work's tortuosity (Fig. 1c). From the perspective of CL tortuosity, this indicates an already well-engineered HC electrode in terms of ionomer distribution. Nevertheless, PFSA-based electrodes can efficiently operate with a high ionomer

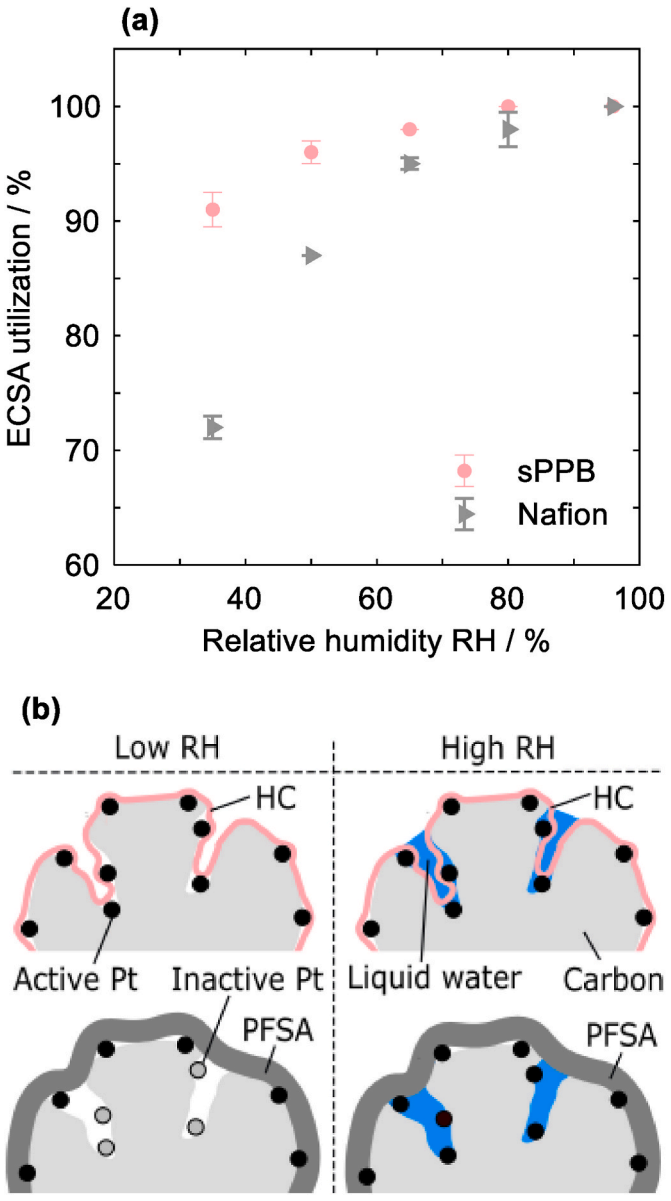

Fig. 3. (a) Measured ECSA utilization in the cathode CL for sPPB- (I/C = 0.2) and Nafion-based cathodes (I/C = 0.8) with respect to different RHs. An ECSA utilization of 100 % was assumed at 96 % RH. The ECSA measurements were conducted at 80 °C and ambient pressure. (b) Schematic illustrating the potential distribution of thin HC and PFSA films within a high surface area carbon system. At high RH levels (bottom) with condensed water present, all buried Pt particles are accessible to protons, facilitated by either liquid water (for PFSAs) and/or ionomer penetrating into the pores (for HCs). At low RH (top), the absence of condensed water results in a loss of protonic bonding of Pt particles in the PFSA-based system, whereas the HC ionomer film covering the buried Pt nanoparticles largely maintains protonic conduction.

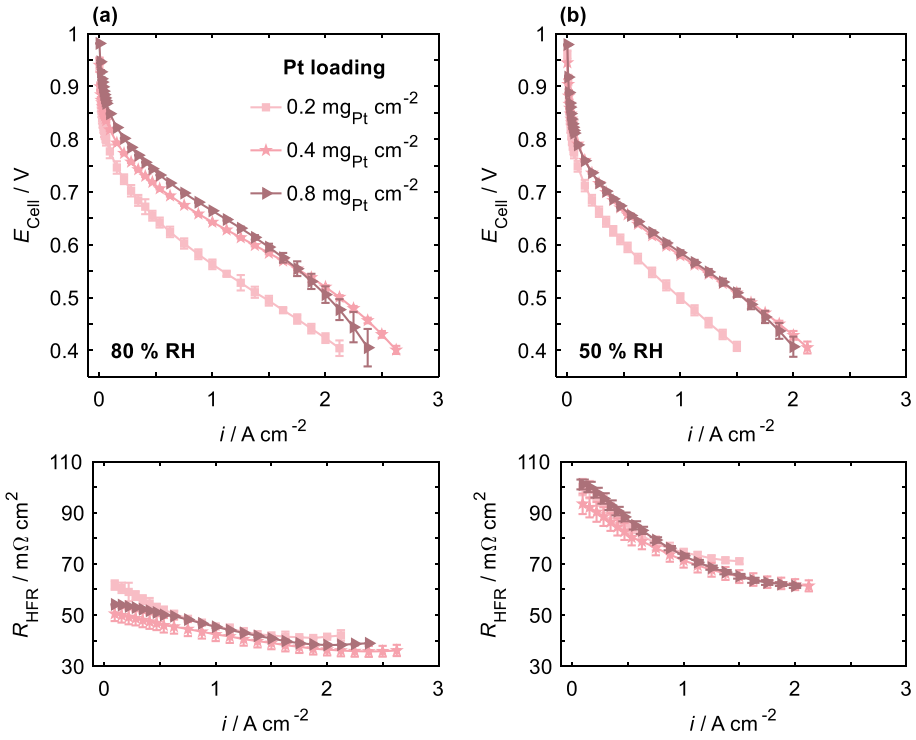

Fig. 4. Polarization curves of fully HC-based cells and associated high frequency resistance R_{HFR} for different Pt loadings of 0.2, 0.4 and 0.8 mg_{Pt} cm^{-2} at 95 °C, 250 kPa_{abs} and (a) 80 % RH or (b) 50 % RH.

volume fraction (due to intrinsically high gas permeability) and achieve a tortuosity of 1 without causing significant overall performance losses at RHs less than or equal to 50 % [24]. At these low RHs, HC-based electrodes with a tortuosity of 1 (i.e., I/C = 0.4 or higher) show increased gas transport resistance and, thus, yield low performance [23]. On the other hand, gas transport optimized HC-based electrodes [15] (i.e., I/C = 0.2 at 0.4 mg_{Pt} cm^{-2}) exhibit a poorly percolated ionomer network and/or restrict the formation of thicker, potentially higher conductive ionomer thin films.

The following sections examine the severe implications of these limitations for the protonic conductivity of HC-based CLs. Improvement approaches that go beyond the apparent ionomer redesign towards higher intrinsic conductivity (and gas permeability) are discussed and verified with a proof of concept.

Current distribution and Pt utilization in HC-based electrodes. — The resistance to proton transport within the cathode CL leads to a drop in potential across the thickness of the electrode [48]. Consequently, the generated ORR current i_{ORR} is a function of the coordinate x across the electrode, with $x = 0$ at the membrane/CL interface and $x = \delta_{CL}$ at the CL/gas diffusion media interface. Based on the work of Neyerlin et al. [22], the distribution of $i_{ORR}(x)$ within the CL can be estimated for known parameters of the cathodes protonic resistance $R_{H^+}^{cathode}$, the electrode's thickness δ_{CL}, Tafel slope (TS) and the applied average current density i. As simple Tafel kinetics and negligible gas transport resistance are assumed, the model holds true for rather small values of i. Normalized to an average current density of $i = 50\ mA\ cm^{-2}$, distributions of i_{ORR} along the thickness coordinate x across the cathode CL were calculated for both sPPB- (Fig. 2a) and Nafion-based cathode CLs (Fig. 2b) at different RHs. To allow for a better comparison, x was normalized to the thickness of the cathode CL. A single intrinsic TS of 70 mV dec^{-1} with a cathodic transfer coefficient of 1 was assumed. Although the in-situ measured Tafel slopes are slightly higher for both ionomers (Table 1), they might still be influenced by an unaccounted mass transport resistance and thus may not accurately represent true ORR kinetics [34,49].

For 80 % RH, both cathodes, using either sPPB or Nafion as an ionomer, show an almost constant dimensionless current density distribution of the ORR along the thickness of the CL. Reducing RH increases the protonic resistance, leading to a higher phase potential drop across the electrode. Consequently, a lower local $i_{ORR}(x)$ is observed farther away from the membrane. In comparison to Nafion, the HC-based cathode demonstrates a highly non-uniform normalized current density distribution at RHs below 50 %. At these low RH levels, over 80 % of the ORR current is generated within the first half of the hydrocarbon CL, leading to low Pt utilization. Originating from the phase potential drop across the electrode, the Pt utilization u was calculated for all different RHs (Fig. 2c) [22]. For both sPPB- and Nafion-based electrodes, u is maximized at the highest level of external humidification (i.e., $u \geq 92$ % at 96 % RH). Under this condition, the catalyst is functioning close to its maximum capability over the entire cathode CL. Thus, the extracted kinetic values in Table 1, used for calculating the various current density distributions and Pt utilizations, present 'true' kinetics to a high extend, with minimal influence from the cathode's protonic resistance [22]. With a decrease in RH, the Pt utilization drops rather sharply for electrodes fabricated from sPPB compared to Nafion. Under the targeted low-humidified operating conditions (RH ≤ 50 %), u_{sPPB} is less than or equal to 13 %, rendering it even more challenging to match the performance of the fully Nafion-based reference cell, which has more than four times higher Pt utilization.

The calculation of protonic resistance-induced Pt utilization assumes that Pt nanoparticles are consistently protonically connected. This correlation has the highest robustness when the ECSA is fully utilized, which is considered to be the case under fully humidified conditions [50]. Despite the use of high surface area carbons with Pt nanoparticles embedded within the inside of primary particles [51], a relatively minor impact of the humidity on ECSA was observed for sPPB-based CLs (Fig. 3a). The ECSA decreases from 100 % to 91 % when reducing the RH from 96 % to 35 %. In contrast, the Nafion-based reference exhibits a significant correlation between the ECSA and RH, consistent with findings in the literature [50,52,53]. This correlation is typically attributed to the absence of condensed water (i.e., reduced RH) within the

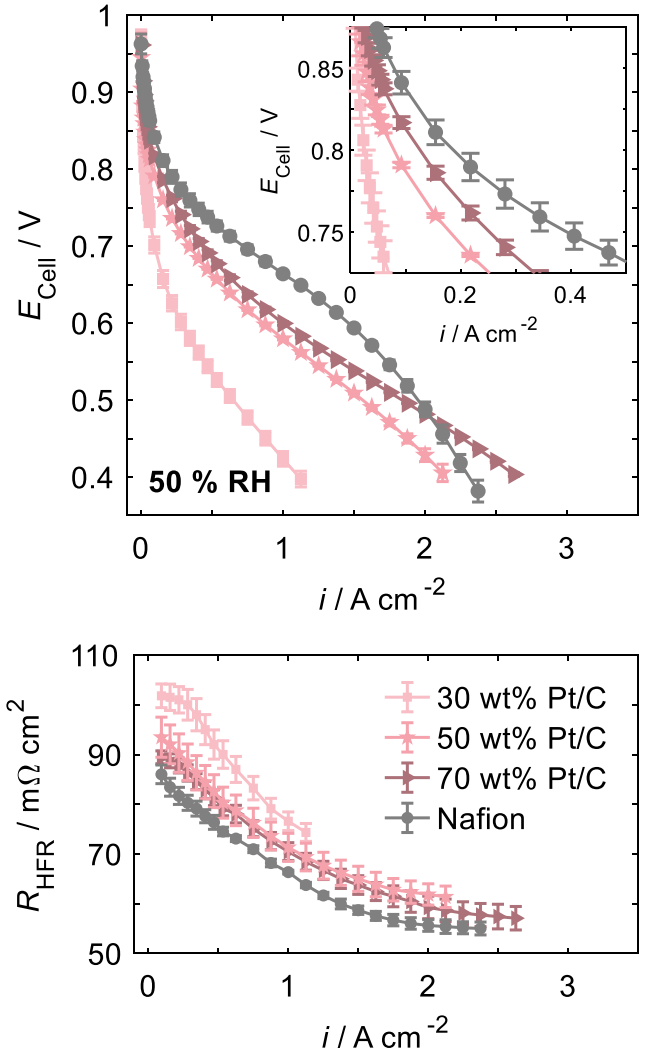

Fig. 5. Polarization curves and high frequency resistance measurements R_{HFR} of fully HC-based CCMs utilizing Pemion® HNN8 in the electrodes. A constant I/C ratio of 0.2 and Pt loading of 0.4/0.1 mg_{Pt} cm^{-2} on cathode/anode was maintained, while the Pt/C ratio was varied from 30 % to 70 %. Measurements were conducted at 95 °C, 250 kPa_{abs} 50 % RH. A fully PFSA-based CCM with Nafion D2020 (I/C = 0.8) as an electrode ionomer is displayed for comparison (i.e., same Pt loading compared to HC-based CCMs, 50 % Pt/C ratio).

nanopores of the carbon particles [50]. The absence of liquid water impedes the formation of a proton-conductive pathway towards the buried Pt particles, which lack direct ionomer coverage. While it is beyond the scope of this work to fully clarify the differences in RH-dependent ECSA utilization between HC- and PFSA-based electrodes, we propose the penetration of ionomer into the nanopores of the primary particles as a potential explanation (Fig. 3b). PFSAs form dispersions with the corresponding solvent composition affecting their aggregation [54–56], whereas HCs are assumed to form 'true' solutions within the ink system over a wide range of alcohol water mixtures [57]. Consequently, the ionomer penetrates into the mesopores contacting the Pt particles inside, in contrast to PFSA ionomers, which leave those particles disconnected. This could explain why the ECSA of the HC ionomer-based CLs remains high regardless of RH up to a certain point, while the PFSA-based CLs do show a strong dependency as they require water for transporting protons to reach the nanoparticles inside the mesopores. However, further investigations are required to validate this hypothesis.

As a first conclusion, HC-based electrodes, with their gas transport

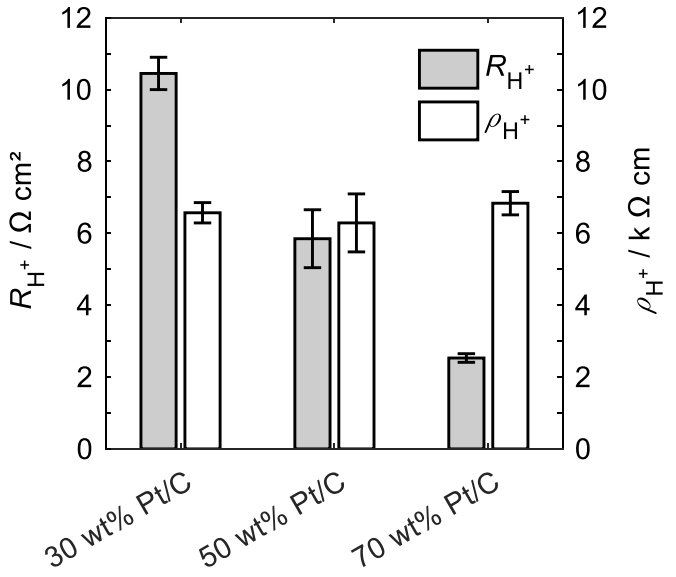

Fig. 6. Protonic resistance R_{H^+} and protonic resistivity ρ_{H^+} at a relative humidity of 50 % for three HC-based cathodes containing different Pt/C ratios.

Table 2
Comparison between cathode CLs, utilizing Nafion D2020 and Pemion® HNN8. All cathodes featured a constant Pt loading of 0.4 ± 0.015 mg_{Pt} cm^{-2}. The HC-based cathodes differ with respect to their Pt/C ratio and thus with the thickness δ_{CL} of the CL. The current density i was extracted at 50 % RH and 0.75 V from Fig. 5a. The mass activity i_m was tested under fully humidified conditions, H_2/O_2 gas flows (0.2 slpm/1 slpm), 150 kPa_{abs} and 80 °C, whereas the ECSA was examined under 96 % RH, H_2/N_2 gas flows (0.2 slpm/0 slpm) at 40 °C and ambient pressure.

Cathode ionomer	I/C ratio | Pt/C ratio	ECSA (m^2 g^{-1})	δ_{CL} (μm)	i (mA cm^{-2}) at 0.75 V and 50 % RH	R_{H^+} (Ω cm^2) at 50 % RH	i_m (A g^{-1})
Nafion	0.8 | 50 wt% Pt/C	72 ± 2	9.6 ± 0.7	393 ± 18	0.7 ± 0.1	83 ± 5
HNN8	0.2 | 30 wt% Pt/C	82 ± 2	15.9 ± 0.5	50 ± 7	10.5 ± 0.5	52 ± 3
HNN8	0.2 | 50 wt% Pt/C	66 ± 3	9.3 ± 0.5	180 ± 3	5.9 ± 0.8	47 ± 3
HNN8	0.2 | 70 wt% Pt/C	48 ± 1	3.7 ± 0.6	251 ± 11	2.5 ± 0.1	43 ± 3

resistance limiting the possibility of increasing the 'standard' I/C ratio of 0.2 to higher values with less protonic resistance, suffer at low RHs from a non-homogeneous current distribution along the thickness of the CL. Consequently, Pt utilization in HC-based electrodes is inferior compared to PFSAs, with these trends exacerbated at higher drawn currents. Nevertheless, the reliability of the model at low RH remains uncertain, as it neglects the overpotential from the anode and relies on protonic resistance data extracted assuming a homogeneous distributed one-dimensional H_2/N_2 transmission-line model across the electrode [58, 59]. To validate the model, polarization curves with three different cathode CL thicknesses, achieved by varying the Pt loading from 0.2 mg_{Pt} cm^{-2} to 0.8 mg_{Pt} cm^{-2}, were recorded for 80 % RH (Fig. 4a) and 50 % RH (Fig. 4b), using Pemion® HNN8 as electrode electrolyte.

At 80 % RH, where the protonic resistance is sufficiently low to almost fully utilize the catalyst layer (see Fig. 2), increasing the Pt loading is directly linked to improved performance – with exception of

the high current density area, which is affected by mass transport issues stemming from thicker electrode layers coming along with a higher Pt loading. However, at 50 % RH, the overall cell performance only improves with an increase of the Pt loading from 0.2 mg_{Pt} cm^{-2} to 0.4 mg_{Pt} cm^{-2}, where the model already predicts barely any contribution of Pt nanoparticles near the GDL/MPL interface to the overall ORR-current generation. Further increase of the Pt loading (0.8 mg_{Pt} cm^{-2}) does not impact the performance positively and yields a virtually identical polarization curve. Thus, the model's simple analytic expressions for the dimensionless ORR current density distribution and the Pt utilization are qualitatively valid, predicting verifiable results for both low and high humidified scenarios. Given that electrodes with a thickness determined by Pt/C ratio and Pt loading (i.e., 50 wt% Pt/C and 0.4 mg_{Pt} cm^{-2}) appear to show minimal ORR current near the CL/gas diffusion media interface at low RHs, the engineering of thinner CLs was analyzed as a potential solution to increase Pt utilization of HC electrodes.

HC-based fuel cell performance with reduced CL thickness. — As predicted by the model, reducing the thickness of HC-based catalyst layer by increasing the Pt/C ratio, leads to improved fuel cell performance at low humidified conditions (Fig. 5a). For all CCMs, a constant I/C ratio of 0.2 and Pt loading of 0.4 mg_{Pt} cm^{-2} was maintained.

At 50 % RH, utilizing the "standard" 50 wt% Pt/C ratio in the cathode CL, employed in this and other studies involving HC ionomers [13,15,60], increases the overall fuel cell performance significantly when compared to cathode CLs consisting of 30 wt% Pt/C ratio. Specifically, the current density at 0.75 V and 50 % RH is more than three times higher. Thereby, the CL thickness behaves inversely to the Pt/C ratio (see supporting information, Fig. S6), increasing from 9.3 μm (50 wt% Pt/C ratio) to 15.9 μm (30 wt% Pt/C ratio). The overall highest fuel cell performance was generated with the thinnest cathode CLs tested (i.e., 70 wt% Pt/C ratio, 3.7 μm). The detailed analysis confirms the expected correlation of performance increase with the reduction in the cathode's protonic resistance. When transitioning from a Pt/C ratio of 30 wt% to 70 wt%, the protonic resistance R_{H^+} decreased by a factor of 4. However, the protonic resistivity ρ_{H^+} remains almost constant, as one would expect, unaffected by changes in the cathode thickness (Fig. 6). The considerable reduction in cathode CL thickness is also expected to reduce the overall gas transport resistance, as the diffusional driven transport resistances (i.e., molecular and Knudsen diffusion) are known to scale with the effective thickness of the CL [61]. Both the reduced protonic resistance and gas transport resistance counteract the rise in kinetic overpotential (i.e., a reduction in mass activities), when increasing the Pt/C ratio. This decrease in mass activity could be attributed to the ECSA, which is lowest for cathodes utilizing a Pt/C ratio of 70 wt% (Table 2). The correlation of an ECSA decrease with increasing Pt/C ratio is in line with literature and attributable to larger Pt particles with less surface area [62].

With the performance achieved at 50 % RH, we establish a benchmark comparable to the approach of gradient ionomer content within the cathode CL by Nguyen et al. [15] where highly active PtCo/C and a membrane with lower HFR was used. Nevertheless, a persisting performance gap compared to fully PFSA-based CLs remains (Fig. 5).

4. Conclusion

This study elucidated the understanding of why the protonic resistance of hydrocarbon- (HC-) based catalyst layers (CLs) is higher at low relative humidity (RH) when compared to PFSA-based references. The reasons for this difference can be summarized to: i) lower hydrocarbon ionomer bulk conductivity; ii) lower water uptake and conductivity of thin hydrocarbon ionomer films compared to bulk ionomer; iii) low hydrocarbon ionomer gas permeability, which limits the maximum ionomer volume fraction within the CL; iv) increased hydrocarbon ionomer tortuosity for such low ionomer volume fractions. The consequence is a non-homogeneous ORR current distribution across the CL, where catalyst close to the gas diffusion medium barely contributes to the overall reaction.

In terms of electrode engineering, the relevance of forming a 'true solution' vs. an ionomer dispersion within the ink system is emphasized by two independent findings: i) hydrocarbon-based CLs exhibit slightly lower tortuosity than PFSA-based CLs at the same ionomer volume fraction; ii) the ECSA appears to be less dependent on RH in HC cathodes compared to PFSA-based cathodes, when utilizing a high surface area carbon support. Both observations could be attributed to a more pervasive ionomer distribution for hydrocarbons, possibly enabled through a true solution with ionomer penetration even into mesopores.

While the ECSA-based catalyst utilization is in favor of hydrocarbon-based CLs, the catalyst utilization originating from the protonic resistance induced potential drop across the CL is severely detrimental in comparison to PFSA. If hydrocarbon ionomers do not significantly improve in terms of oxygen permeability to enable higher volume fractions in the CL, we suggest developing thinner CLs to achieve a better balance between low protonic and gas transport resistance. A proof of concept is provided within this work, where reducing the electrode thickness is achieved by altering the Pt/C ratio from 50 wt% to 70 wt% (by keeping the same I/C ratio and absolute Pt loading). This adjustment reduces the cathode's protonic resistance by 50 %, while increasing the power density at 0.75 V by about 40 %. Further efforts in engineering thin hydrocarbon-based CLs may constitute the first steps to overcome the tradeoff between low protonic resistance and low mass transport resistance towards closing the performance gap to PFSA-based cells.

CRediT authorship contribution statement

Hannes Liepold: Writing – original draft, Visualization, Methodology, Investigation, Formal analysis, Conceptualization. **Ashley Bird:** Writing – original draft, Methodology, Investigation. **Philipp A. Heizmann:** Writing – review & editing, Writing – original draft, Visualization, Methodology. **Hassan Fadlullah:** Investigation. **Hien Nguyen:** Writing – review & editing, Conceptualization. **Carolin Klose:** Writing – review & editing, Supervision, Resources. **Steven Holdcroft:** Writing – review & editing, Resources. **Ahmet Kusoglu:** Writing – review & editing, Supervision, Resources. **Severin Vierrath:** Writing – review & editing, Supervision, Resources. **Andreas Münchinger:** Writing – review & editing, Visualization, Supervision, Conceptualization.

Declaration of competing interest

The authors declare that they have no known competing financial interests or personal relationships that could have appeared to influence the work reported in this paper.

Data availability

Data will be made available on request.

Acknowledgements

The authors acknowledge funding from BMDV within the project 'H2Sky' (Grant No. 03B10706G). Additionally, A. Kusoglu and A. Bird acknowledge the funding from M2FCT, U.S. Department of Energy (DOE), Office of Energy Efficiency and Renewable Energy, Hydrogen and Fuel Cell Technologies Office: Contract number DE-AC02-05CH11231.

Appendix A. Supplementary data

Supplementary data to this article can be found online at https://doi.org/10.1016/j.jpowsour.2024.235537.

References

[1] D.A. Cullen, K.C. Neyerlin, R.K. Ahluwalia, R. Mukundan, K.L. More, R.L. Borup, A. Z. Weber, D.J. Myers, A. Kusoglu, Nat. Energy 6 (5) (2021) 462–474.
[2] A. Kusoglu, A.Z. Weber, Chem. Rev. 117 (3) (2017) 987–1104.
[3] V. Rao, N. Kluy, W. Ju, U. Stimming, in: A.K. Pabby, S.S. Rizvi, A.M.S. Requena (Eds.), Handbook of Membrane Separations, CRC Press, Boca Raton, Florida, 2015, p. 524.
[4] M. Adamski, N. Peressin, S. Holdcroft, Mater. Adv. 2 (15) (2021) 4966–5005.
[5] D.W. Shin, M.D. Guiver, Y.M. Lee, Chem. Rev. 117 (6) (2017) 4759–4805.
[6] C. Sonne, B.M. Jenssen, J. Rinklebe, S.S. Lam, M. Hansen, R. Bossi, K. Gustavson, R. Dietz, Sci. Total Environ. 876 (2023) 162770.
[7] X. Lim, Nature 620 (7972) (2023) 24–27.
[8] V. Ramani, S. Swier, M.T. Shaw, R.A. Weiss, H.R. Kunz, J.M. Fenton, J. Electrochem. Soc. 155 (6) (2008) B532.
[9] M. Hwang, K. Nixon, R. Sun, C. Willis, Y.A. Elabd, J. Membr. Sci. 633 (2021) 119330.
[10] J.E. Chae, S.J. Yoo, J.Y. Kim, J.H. Jang, S.Y. Lee, K.H. Song, H.-J. Kim, Int. J. Hydrogen Energy 45 (57) (2020) 32856–32864.
[11] S. Xu, M. Adamski, M. Killer, E.M. Schibli, B.J. Frisken, S. Holdcroft, Macromolecules 52 (6) (2019) 2548–2559.
[12] E. Balogun, M. Adamski, S. Holdcroft, J. Electrochem. Soc. 167 (8) (2020) 84502.
[13] E. Balogun, S. Cassegrain, P. Mardle, M. Adamski, T. Saatkamp, S. Holdcroft, ACS Energy Lett. 7 (6) (2022) 2070–2078.
[14] H. Nguyen, F. Lombeck, C. Schwarz, P.A. Heizmann, M. Adamski, H.-F. Lee, B. Britton, S. Holdcroft, S. Vierrath, M. Breitwieser, Sustain. Energy Fuels 5 (14) (2021) 3687–3699.
[15] H. Nguyen, D. Sultanova, P.A. Heizmann, S. Vierrath, M. Breitwieser, Mater. Adv. 3 (23) (2022) 8460–8468.
[16] H. Nguyen, J. Stiegeler, H. Liepold, C. Schwarz, S. Vierrath, M. Breitwieser, Energ. Tech. 11 (8) (2023).
[17] H. Nguyen, C. Klose, L. Metzler, S. Vierrath, M. Breitwieser, Adv. Energy Mater. 12 (12) (2022) 2103559.
[18] M. Teliska, V.S. Murthi, S. Mukerjee, D.E. Ramaker, J. Phys. Chem. C 111 (26) (2007) 9267–9274.
[19] M. Adamski, T.J.G. Skalski, B. Britton, T.J. Peckham, L. Metzler, S. Holdcroft, Angew. Chem. 56 (31) (2017) 9058–9061.
[20] D. Yazili, E. Marini, T. Saatkamp, A. Münchinger, T. de Wild, L. Gubler, G. Titvinidze, M. Schuster, C. Schare, L. Jörissen, K.-D. Kreuer, J. Power Sources 563 (2023) 232791.
[21] C. Klose, T. Saatkamp, A. Münchinger, L. Bohn, G. Titvinidze, M. Breitwieser, K.-D. Kreuer, S. Vierrath, Adv. Energy Mater. 10 (14) (2020).
[22] K.C. Neyerlin, W. Gu, J. Jorne, A. Clark, H.A. Gasteiger, J. Electrochem. Soc. 154 (2) (2007) B279.
[23] H. Liepold, H. Nguyen, P.A. Heizmann, C. Klose, S. Vierrath, A. Münchinger, J. Electrochem. Soc. 171 (5) (2024) 54509.
[24] Y. Liu, M.W. Murphy, D.R. Baker, W. Gu, C. Ji, J. Jorne, H.A. Gasteiger, J. Electrochem. Soc. 156 (8) (2009) B970.
[25] H. Liu, L. Ney, N. Zamel, X. Li, Appl. Sci. 12 (8) (2022) 3776.
[26] T. Morawietz, M. Handl, C. Oldani, P. Gazdzicki, J. Hunger, F. Wilhelm, J. Blake, K. A. Friedrich, R. Hiesgen, J. Electrochem. Soc. 165 (6) (2018) F3139–F3147.
[27] S. Holdcroft, Chem. Mater. 26 (1) (2014) 381–393.
[28] K. Karan, Curr. Opin. Electrochem. 5 (1) (2017) 27–35.
[29] D.K. Paul, R. McCreery, K. Karan, J. Electrochem. Soc. 161 (14) (2014) F1395–F1402.
[30] K. Karan, Langmuir: ACS J. Surface. Colloid. 35 (42) (2019) 13489–13520.
[31] Z. Siroma, R. Kakitsubo, N. Fujiwara, T. Ioroi, S. Yamazaki, K. Yasuda, J. Power Sources 189 (2) (2009) 994–998.
[32] T.J.G. Skalski, B. Britton, T.J. Peckham, S. Holdcroft, J. Am. Chem. Soc. 137 (38) (2015) 12223–12226.
[33] J. Xie, F. Xu, D.L. Wood, K.L. More, T.A. Zawodzinski, W.H. Smith, Electrochim. Acta 55 (24) (2010) 7404–7412.
[34] K.C. Neyerlin, W. Gu, J. Jorne, H.A. Gasteiger, J. Electrochem. Soc. 153 (10) (2006) A1955.
[35] I. Arganda-Carreras, V. Kaynig, C. Rueden, K.W. Eliceiri, J. Schindelin, A. Cardona, H. Sebastian Seung, Bioinformatics 33 (15) (2017) 2424–2426.
[36] A. Bird, M. Lindell, D.I. Kushner, A. Haug, M. Yandrasits, A. Kusoglu, Adv. Funct. Mater. 34 (27) (2024) 2311073.
[37] D. Sharon, P. Bennington, C. Liu, Y. Kambe, B.X. Dong, V.F. Burnett, M. Dolejsi, G. Grocke, S.N. Patel, P.F. Nealey, J. Electrochem. Soc. 165 (16) (2018) H1028–H1039.
[38] M.A. Modestino, D.K. Paul, S. Dishari, S.A. Petrina, F.I. Allen, M.A. Hickner, K. Karan, R.A. Segalman, A.Z. Weber, Macromolecules 46 (3) (2013) 867–873.
[39] D.K. Paul, J.B. Giorgi, K. Karan, J. Electrochem. Soc. 160 (4) (2013) F464–F469.
[40] K.R. Cooper, J. Electrochem. Soc. 157 (11) (2010) B1731.
[41] M. Adamski, T.J. Skalski, E.M. Schibli, M. Killer, Y. Wu, N. Peressin, B.J. Frisken, S. Holdcroft, J. Membr. Sci. 595 (2020) 117539.
[42] M.F. Mathias, R. Makharia, H.A. Gasteiger, J.J. Conley, T. Fuller, C. Gittleman, S. S. Kocha, Electrochem. Soc. Interface 14 (3) (2005) 24–35.
[43] C.C. de Araujo, K.D. Kreuer, M. Schuster, G. Portale, H. Mendil-Jakani, G. Gebel, J. Maier, Phys. Chem. Chem. Phys. : Phys. Chem. Chem. Phys. 11 (17) (2009) 3305–3312.
[44] M. Schuster, K.-D. Kreuer, H.T. Andersen, J. Maier, Macromolecules 40 (3) (2007) 598–607.
[45] V.J. Bharath, J. Millichamp, T.P. Neville, T.J. Mason, P.R. Shearing, R. Brown, G. Manos, D. Brett, J. Membr. Sci. 497 (2016) 229–238.
[46] D.I. Kushner, A. Kusoglu, N.J. Podraza, M.A. Hickner, Adv. Funct. Mater. 29 (37) (2019).
[47] M. Sabharwal, L.M. Pant, A. Putz, D. Susac, J. Jankovic, M. Secanell, Fuel Cell. 16 (6) (2016) 734–753.
[48] M. Eikerling, A.A. Kornyshev, J. Electroanal. Chem. 453 (1–2) (1998) 89–106.
[49] T. Lazaridis, H.A. Gasteiger, J. Electrochem. Soc. 168 (11) (2021) 114517.
[50] R. Girod, T. Lazaridis, H.A. Gasteiger, V. Tileli, Nat. Catal. 6 (5) (2023) 383–391.
[51] V. Yarlagadda, M.K. Carpenter, T.E. Moylan, R.S. Kukreja, R. Koestner, W. Gu, L. Thompson, A. Kongkanand, ACS Energy Lett. 3 (3) (2018) 618–621.
[52] N. Ramaswamy, W. Gu, J.M. Ziegelbauer, S. Kumaraguru, J. Electrochem. Soc. 167 (6) (2020) 64515.
[53] P. Schneider, A.-C. Scherzer, B.D. Storey, M. Klingele, N. Zamel, D. Gerteisen, J. Electrochem. Soc. 170 (10) (2023) 104505.
[54] S.A. Berlinger, P.J. Dudenas, A. Bird, X. Chen, G. Freychet, B.D. McCloskey, A. Kusoglu, A.Z. Weber, ACS Appl. Polym. Mater. 2 (12) (2020) 5824–5834.
[55] T. van Cleve, S. Khandavalli, A. Chowdhury, S. Medina, S. Pylypenko, M. Wang, K. L. More, N. Kariuki, D.J. Myers, A.Z. Weber, S.A. Mauger, M. Ulsh, K.C. Neyerlin, ACS Appl. Mater. Interfaces 11 (50) (2019) 46953–46964.
[56] A. Chowdhury, A. Bird, J. Liu, I.V. Zenyuk, A. Kusoglu, C.J. Radke, A.Z. Weber, ACS Appl. Mater. Interfaces 13 (36) (2021) 42579–42589.
[57] J. Peron, Z. Shi, S. Holdcroft, Energy Environ. Sci. 4 (5) (2011) 1575.
[58] R. Makharia, M.F. Mathias, D.R. Baker, J. Electrochem. Soc. 152 (5) (2005) A970.
[59] T. Gaumont, G. Maranzana, O. Lottin, J. Dillet, S. Didierjean, J. Pauchet, L. Guétaz, Int. J. Hydrogen Energy 42 (3) (2017) 1800–1812.
[60] E. Balogun, P. Mardle, H. Nguyen, M. Breitwieser, S. Holdcroft, Electrochim. Acta 401 (2022) 139479.
[61] N. Nonoyama, S. Okazaki, A.Z. Weber, Y. Ikogi, T. Yoshida, J. Electrochem. Soc. 158 (4) (2011) B416.
[62] S.A. Berlinger, A. Chowdhury, T. van Cleve, A. He, N. Dagan, K.C. Neyerlin, B. D. McCloskey, C.J. Radke, A.Z. Weber, ACS Appl. Mater. Interfaces 14 (32) (2022) 36731–36740.